Delft University of Technology

Achieving superelasticity in additively manufactured Ni-lean NiTi by crystallographic design

Zhu, Jia Ning; Liu, Kai; Riemslag, Ton; Tichelaar, Frans D.; Borisov, Evgenii; Yao, Xiyu; Popovich, Anatoly; Huizenga, Richard; Hermans, Marcel; Popovich, Vera

DOI
10.1016/j.matdes.2023.111949

Publication date
2023

Document Version
Final published version

Published in
Materials and Design

Citation (APA)
Zhu, J. N., Liu, K., Riemslag, T., Tichelaar, F. D., Borisov, E., Yao, X., Popovich, A., Huizenga, R., Hermans, M., & Popovich, V. (2023). Achieving superelasticity in additively manufactured Ni-lean NiTi by crystallographic design. *Materials and Design*, *230*, Article 111949. https://doi.org/10.1016/j.matdes.2023.111949

Important note
To cite this publication, please use the final published version (if applicable).
Please check the document version above.

Copyright
Other than for strictly personal use, it is not permitted to download, forward or distribute the text or part of it, without the consent of the author(s) and/or copyright holder(s), unless the work is under an open content license such as Creative Commons.

Takedown policy
Please contact us and provide details if you believe this document breaches copyrights.
We will remove access to the work immediately and investigate your claim.

This work is downloaded from Delft University of Technology.
For technical reasons the number of authors shown on this cover page is limited to a maximum of 10.

Materials & Design 230 (2023) 111949

Contents lists available at ScienceDirect

Materials & Design

journal homepage: www.elsevier.com/locate/matdes

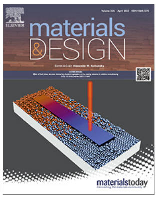

Achieving superelasticity in additively manufactured Ni-lean NiTi by crystallographic design

Jia-Ning Zhu [a,*], Kai Liu [a], Ton Riemslag [a], Frans D. Tichelaar [b], Evgenii Borisov [c], Xiyu Yao [d], Anatoly Popovich [c], Richard Huizenga [a], Marcel Hermans [a], Vera Popovich [a,*]

[a] Faculty of Mechanical, Maritime, and Materials Engineering, Delft University of Technology, The Netherlands
[b] Kavli Institute of Technology, Quantum Nanoscience, Delft University of Technology, The Netherlands
[c] Peter the Great Saint-Petersburg Polytechnic University, Saint Petersburg, Russia
[d] Department of Materials Science and Engineering, Southern University of Science and Technology, Shenzhen 518055, China

HIGHLIGHTS

- An atomistic-to-mesoscale modelling framework is proposed for designing high-performance NiTi.
- The designed ⟨001⟩ textured NiTi was successfully fabricated by additive manufacturing.
- An unprecedented superelasticity up to 453 K with a high and wide temperature window (110 K) in Ni-lean NiTi was achieved.

GRAPHICAL ABSTRACT

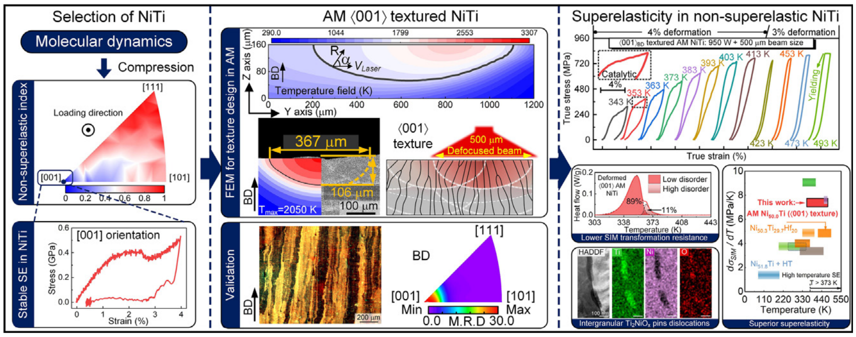

ARTICLE INFO

Article history:
Received 21 January 2023
Revised 29 March 2023
Accepted 20 April 2023
Available online 2 May 2023

Keywords:
Shape memory alloys
Superelasticity
Laser powder bed fusion
Anisotropy
NiTi

ABSTRACT

Superelastic metallic materials possessing large recoverable strains are widely used in automotive, aerospace and energy conversion industries. Superelastic materials working at high temperatures and with a wide temperature range are increasingly required for demanding applications. Until recently, high-temperature superelasticity has only been achievable with multicomponent alloys fabricated by complex processes. In this study, a novel framework of multi-scale models enabling texture and microstructure design is proposed for high-performance NiTi fabrication via laser powder bed fusion. Based on the developed framework, a Ni-lean Ni(49.4 at.%)-Ti alloy is, for the first time, endowed with a 4% high-temperature compressive superelasticity. A ⟨001⟩ texture, unfavorable for plastic slip, is created to realize enhanced functionality. The unprecedented superelasticity can be maintained up to 453 K, which is comparable with but has a wider superelastic temperature range (~110 K) than rare earth alloyed NiTi alloys, previously only realizable with grain refinement, and other complicated post-processing operations. At the same time, its shape memory stability is also improved due to existing textured ⟨100⟩ martensite and intergranular precipitation of Ti_2NiOx. This discovery reframes the way that we design superior performance NiTi based alloys through directly tailoring crystallographic orientations during additive manufacturing.

© 2023 The Author(s). Published by Elsevier Ltd. This is an open access article under the CC BY license (http://creativecommons.org/licenses/by/4.0/).

---

* Corresponding authors.
E-mail addresses: J.Zhu-2@tudelft.nl (J.-N. Zhu), V.Popovich@tudelft.nl (V. Popovich).

https://doi.org/10.1016/j.matdes.2023.111949
0264-1275/© 2023 The Author(s). Published by Elsevier Ltd.
This is an open access article under the CC BY license (http://creativecommons.org/licenses/by/4.0/).

1. Introduction

Reversible martensitic transformation, a diffusionless solid–solid phase transition [1], gives shape memory alloys (SMAs) unique functional properties. Depending on the initial phase states before deformation, the properties are divided into superelasticity and shape memory effect (SME). Superelasticity (also termed pseudoelasticity), a rubber-like behavior, makes SMAs recover their deformation after unloading [2]. Unlike traditional metallic materials, superelastic SMAs can recover several percent of strain. SME is a capability of SMAs to regain their original shapes after deformation by heating [3]. Due to its attractive functional properties [4,5], SMAs are widely utilized as actuators, sensors, dampers and medical implants [6]. However, superelasticity with higher operating temperatures and a wider superelastic temperature is required [7] in such emerging applications as aerospace, energy and vehicle engineering fields. At the same time, to improve energy utilizing efficiency and reduce costs, SMAs with multi-functions, a high-temperature superelasticity and a stable SME, are highly desired.

Nitinol (NiTi), as the most commercially successful shape memory alloy, cannot meet this challenge. Traditionally, high-temperature superelasticity has been achieved by increasing phase-transformation temperatures whilst inhibiting dislocation slip through lattice distortion [8], grain refinement [9] or precipitation strengthening [10]. These require complex processing combinations of multicomponent alloying [7,8], severe-plastic deformation [9] and heat treatments [10,11]. For instance, Ti_{20}-$Hf_{15}Zr_{15}Cu_{25}Ni_{25}$ [8], $Ti_{16.67}Zr_{16.67}Hf_{16.67}Ni_{25}Co_{10}Cu_{15}$ [12] and severely cold rolled Ti-44Ni-5Cu-1Al [13] have been demonstrated to have potential for enhancing high-temperature superelasticity. However, such methods are costly and complex, limiting superelastic products only in form of sheets, tubes and wires.

Nowadays, to minimize greenhouse gas emissions and energy consumption, alloy sustainability should be taken into account. To fulfil this goal, SMAs with simplified alloying components and high superelastic temperature windows need to be developed [14]. It is known that Ni-lean NiTi exhibits martensitic phase transformation in a higher temperature (can reach ~ 373 K) [15], which potentially allows it to achieve high-temperature superelasticity. Nonetheless, due to relatively low yield stress and lack of precipitates blocking dislocation movements, plastic deformation usually occurs prior to stress-induced martensite transformation (SIMT) in the Ni-lean NiTi [16]. Therefore, Ni-lean binary NiTi cannot reveal superelasticity in an as-fabricated state without post-treatments. Limited by conventional processes, traditional concepts of inducing superelasticity is to increase dislocation movement barriers (induced by robust phase interfaces or grain boundaries) [13,17] and improve phase transformation compatibility between austenite and stress-induced martensite [18]. This still inevitably involves multicomponent alloying and complex deformation processes followed by heat treatments.

Crystalline materials can exhibit anisotropic mechanical and functional properties due to preferred crystallographic orientation [19]. Utilizing such anisotropy in Ni-lean NiTi is a promising way to induce high-temperature superelasticity, instead of alloying with rare elements. This introduces a few challenges: 1) is there a preferred crystallographic orientation that can introduce superelasticity in Ni-lean NiTi; 2) how to screen the desirable crystallographic orientation; 3) how to fabricate Ni-lean NiTi with specifically orientated grains. Therefore, quantitative predictions about the effect of crystallographic orientations on NiTi superelasticity and a suitable processing technique should be investigated. Specifically, in the present study, we employed molecular dynamics (MD) in single crystal NiTi to screen appropriate crystallographic orientations for superelastic behavior. Considering the fact that single-crystal fabrication is still challenging, single-crystal-like polycrystalline Ni-lean NiTi consisting of large columnar grains are considered as alternatives [20]. Laser powder bed fusion (L-PBF), a type of an additive manufacturing (AM) technique [21], was applied to fabricate NiTi with designed microstructure. It offers sufficient flexibility to tailor grain morphologies and orientation via tuning L-PBF processing parameters. Furthermore, finite element modeling was carried out to bridge gaps between MD-optimized crystallographic orientations and the design of L-PBF processing parameters.

In this study, for the first time, we report superelasticity with a high and wide temperature window in a Ni-lean Ni(49.4 at.%)-Ti fabricated by additive manufacturing. This was achieved by employing multi-scaled models enabling microstructural design and functional property prediction, which opens up a new way of designing high-performance materials by controlling functional anisotropy.

2. Methodology

2.1. Molecular dynamics simulations

Molecular dynamic (MD) simulations were performed on an open-source code LAMMPS [22]. The modified embedded-atom method (MEAM) potential developed by Ko et al. was applied to describe interatomic interactions [23]. To investigate superelastic behavior at different temperatures, single crystal models, including [1 0 0], [1 1 0], and [1 1 1] orientations, were used. The single crystal model size was ~ 21 × 10.5 × 10.5 nm^3 containing ~ 1.7 × 10^5 atoms. All model sizes slightly varied for each respective configuration to ensure that the model size is an integer multiple of the crystal plane distance. The primitive cell was taken from the literature [24]. To more accurately understand the superelastic behavior in polycrystalline NiTi, the compressive behavior of bicrystal models for [1 0 0], [1 1 0], and [1 1 1] textures were studied. Bicrystal models with nearly the same orientations were built with Atomsk [25], and the model's size was ~ 23 × 16 × 16 nm^3 containing ~ 4.5 × 10^5 atoms. A three-dimensional periodic boundary condition was applied. To simulate the non-elastic deformation in a real material, 0.5% percent of atoms were removed in each model as point defects. After 1 × 10^{-10} s relaxation, the thickness of grain boundaries is about four atomic layers. Phase transformation temperatures were determined by heating and cooling, and the temperature change rate was set as 0.5 K / ps optimized by Ko et al.[23].

Bicrystal models were uniaxially compressed to 4% engineering strain at 353 K, and single crystal models were uniaxially compressed to 8% engineering strain at different temperatures. The length of the simulation box decreases along compressive direction, and sizes along the rest two directions were allowed to expand or shrink to maintain the corresponding stress components near zero. When the compression strain reaches the maximum value, the load was removed and the change of the model's size in the following 2 × 10^{-11} s was recorded. The adaptive common neighbor analysis (A-CNA) is applied to identify the atomic structure during loading, especially the martensitic phase induced by stress which is of most concern. Data analysis and atomic visualizations were carried out on the OVITO [26].

2.2. Finite element modeling

Finite element modeling (FEM) based on heat transfer theory was employed to investigate temperature fields during L-PBF using a COMSOL Multiphysics Modeling software. The corresponding 3D heat conduction equation is:

$$\rho(T)C_p(T)\frac{\partial T}{\partial t} = Q + \nabla(k(T)\nabla T) \tag{1}$$

where $\rho(T)$ (kg m^{-3}) is the temperature-dependent density, $C_p(T)$ (J kg^{-1} K^{-1}) is the temperature-dependent specific heat capacity, $k(T)$ (W m^{-1} k^{-1}) is the temperature-dependent thermal conductivity, Q (W m^{-3}) is the net volumetric heat flux, and v (m s^{-1}) is the laser scanning velocity. The temperature-dependent thermal-physical properties used in this work were calculated by Thermo-Calc software (Version 2020a, Thermo-Calc, Stockholm, Sweden) based on the TCHEA2 (High Entropy Alloys version 2.1) database. Detailed data can be found in our previous work [27]. Material properties in powder layers were scaled based on the powder packing density (0.7 for this work).

Considering that the laser energy can penetrate a certain depth into the powder bed, the volumetric heat flux was expressed as:

$$Q(x,y,z) = \frac{Q_0(x,y)}{\delta}\exp(-\frac{|z|}{\delta}) \tag{2}$$

where Q_0 is the heat flux on the upper surface (W m^{-2}), δ = 65 µm is the optical penetration depth of the material [28], |z| is the absolute value of the z-coordinate. The Gaussian distributed surface heat flux Q_0 is expressed as:

$$Q_0(x,y) = \frac{2AP}{\pi R^2}\exp(-\frac{2((x-vt)^2+y^2)}{R^2}) \tag{3}$$

where P is the laser power, A is the laser absorptivity of the material, and R is the laser beam radius at which the energy density is reduced to 1/e^2 of that at the center of the laser spot. The laser absorptivity A is estimated using the Rosenthal equation based on the experimentally measured melt pool width [29].

2.3. Thermodynamic calculations and grain morphology selection

Classical and solute-trapped Scheil-Gulliver solidification models were simulated using Thermo-Calc software (version 2021b) with the TCHEA2 database. The solution content of Ti in the NiTi BCC_B2 phase as a function of the solid faction was derived from Scheil-Gulliver solidification models.

By utilizing an analytical model, grain morphologies were deduced based on thermal gradient (G) and solidification rate (R). The model is formulated as [30]:

$$\frac{G^n}{R} = a\left\{\sqrt[3]{\frac{-4\pi N_0}{3\ln[1-\varphi]}} \times \frac{1}{n+1}\right\}^n \tag{4}$$

where a = 1.25 × 10^6 (K$^{3.4}$/m·s) and n = 3.4 are material-dependent constants (fitted by the constitutional tip undercooling based on the Thermo-calc TCHEA2 database), N_0 = 2 × 10^{15} m^{-3} is the nuclei density for Ni-based alloys [30] and φ is a grain morphology factor. When morphology mainly consists of columnar grains, φ = 0.05 and if there are equiaxed grains, φ = 0.8. G and R can be calculated based on FEM results.

2.4. Material fabrication

Commercial NiTi (50.0 at% Ni) powder (TLS Technik GmbH, Bitterfeld, Germany) was used to fabricate NiTi parts by means of laser powder bed fusion (L-PBF) under argon protection. NiTi powder consists of spherical particles with D-values of 23 µm (D10), 40 µm (D50), 67 µm (D90) [31]. L-PBF was performed on an Aconity3D Midi (Aconity3D GmbH, Germany) machine equipped with a laser source featuring a maximum power of 1000 W and a beam with a Gaussian power distribution. The optimized L-PBF processing parameters are listed in Table 1. A raster laser scanning pattern with an increment of 67° between each layer was applied to fabricate the NiTi parts.

Table 1
L-PBF process parameters used in this work for NiTi fabrication.

	Non-textured (reference)	$\langle 001\rangle_{BD}$ textured
Laser Power (W), P	250	950
Scan velocity (mm/s), v	1250	1200
Hatch distance (µm), h	120	180
Layer thickness (µm), t	30	50
Laser beam diameter (µm)	80	500
Volumetric energy density (J/mm^3)	56	88

To investigate compressive superelasticity and the SME, cylindrical samples of 13 mm diameter and 25 mm height (along the building direction) were built and then machined into eight compressive cuboids (4 × 4 × 8 mm) using electrical discharge machining (EDM). Samples were ground and polished to remove EDM damage.

2.5. Microstructural characterization

As-fabricated L-PBF samples were cut along the central section parallel to the building direction. Samples were ground and polished according to standard metallographic procedures, followed by etching with two types of reagents. To reveal melt pool boundaries, a HF (3.2 vol%), HNO_3 (14.1 vol%), and H_2O (82.7 vol%) reagent was used. To show the parent austenitic phase, 120 ml distilled water, 15 ml HCl, 15 g $Na_2S_2O_5$, 10 g $K_2S_2O_5$, and 2 g NH_4HF was used. All samples were separately prepared with freshly polished surfaces.

Light optical microscopy with a polarized light was used for the examination of grain morphology. An SEM (JSM-IT100) was used to determine the melt pool shapes and dimensions. Nickel content was analyzed by inductively coupled plasma optical emission spectroscopy (ICP-OES). A micron-scale Ni and Ti elemental distribution map was determined by energy dispersive spectrometry in the scanning electron microscope (SEM JSM-IT100).

An FEI cubed titan Cs-corrected 80–300 kV transmission electron microscopy (TEM) was employed for microstructural characterization at the nano-scale. Elemental mapping was performed and high-angle annular dark field (HAADF) images were produced in a scanning transmission electron microscopy (STEM) mode. TEM samples were mechanically polished to ~ 20 µm thickness, and then punched into 2.3 mm discs and glued on 3 mm diameter Cu rings. The thin disc samples were then further milled to electron transparency by Ar ions.

Phase identification was determined by two-dimensional X-ray diffraction (2D-XRD) using a Bruker D8 Discover diffractometer with Cu Kα radiation and 2D Eiger2 R 500 K detector. Data evaluation was carried out by Bruker software DiffracSuite. EVA vs 5.2. Texture was measured by a Bruker D8 Discover diffractometer with Eulerian cradle in parallel beam geometry with Co Kα radiation. Samples were heated to 373 K by a positive temperature coefficient heating element to ensure an austenitic state. Bruker software DiffracSuite.Diffrac 4.1 was used for Data evaluation.

For in-situ heating and cooling XRD measurements, NiTi samples were first immersed in liquid nitrogen to ensure a fully martensitic state. Temperature changes were achieved by using an Anton Paar DHS 1100 hot-stage with a temperature range from room temperature (RT) to 423 K. XRD scans were measured over a 2θ range between 15° and 100° at RT and between 38° and 150° at 423 K. The scanning step size was 0.04° and the counting time per step was 1 s. The in-situ heating and cooling during XRD were per-

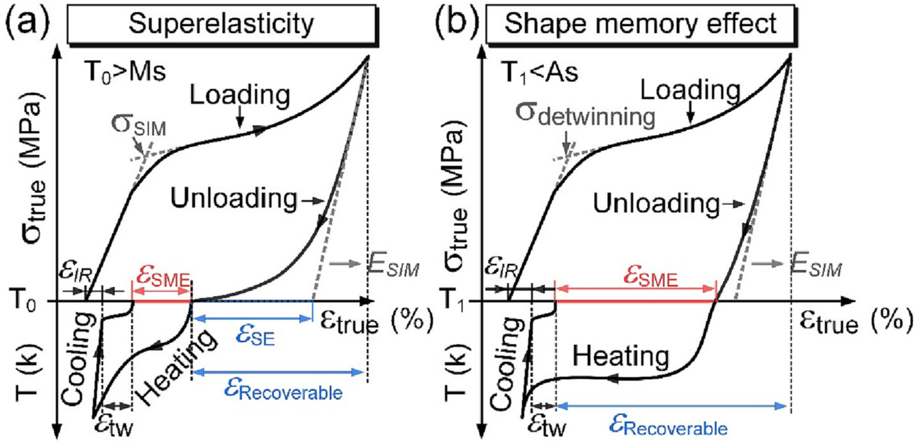

Fig. 1. Schematics of strain definitions and loading path for (a) superelasticity and (b) shape memory effect. Where, T_0 is a testing temperature for superelasticity, T_1 is a testing temperature for shape memory effect, M_s is the martensite starting temperature, A_s is the austenite starting temperature, σ_{SIM} is the critical stress for stress-induced martensite, $\sigma_{detwinning}$ is the critical stress for detwinning, E_{SIM} is the elasticity modulus of stress-induced martensite, ε_{SE} is the superelasticity strain, ε_{SME} is the shape memory effect strain and ε_{IR} is the irreversible strain.

formed using still frames within a 2θ range between 37.6° and 47.0° since martensite B19′ and R phase peaks are mainly located within this range. The counting time per step was 20 s per frame.

For high-temperature texture measurements, four pole figures of NiTi BCC_B2 phase, (1 1 0), (2 0 0), (2 1 1) and (3 1 0) were measured at 423 K. The rotational angle, φ, was scanned from 0 to 360° in steps of 5°. The tilt angle, ψ, was scanned from 0 to 70° in steps of 5°. The harmonic series expansion method was used to obtain the orientation distribution functions (ODFs) and recalculated pole figures. Based on ODFs, the inverse pole figures can be plotted.

Differential scanning calorimetry (DSC) was conducted in a Perkin Elmer DSC 8000 in the temperature range between 203 and 473 K with a heating and cooling rate of 10 K $\min^{-1}$ in order to determine phase transformation temperatures. DSC samples were machined by EDM with a dimension of ϕ 6 mm × 1 mm and extracted from the middle of bulk L-PBF NiTi (cylinders with a dimension of ϕ13 mm × 25 mm).

2.6. Mechanical testing

Superelasticity and shape memory effects were tested on an MTS 858 tabletop hydraulic test machine by applying uniaxial compression. A strain rate of $1.0 \times 10^{-4}\ s^{-1}$ was applied and strains were measured by a contact-based high-temperature ceramic extensometer (632.53F-14, MTS). The temperature change was controlled by induction heating and air flow cooling. The temperature was measured by 3 K-type thermocouples welded onto the NiTi sample surfaces.

Prior to superelasticity tests, samples were heated to 423 K (65 K above austenite finish temperature) and then cooled to 353 K to ensure an austenitic state. Before SME testing, samples were quenched in liquid nitrogen to ensure a fully martensitic state. Schematics of strain definitions and loading paths for superelasticity and the shape memory effect are shown in Fig. 1. Strains were measured by a high-temperature ceramic extensometer. All samples were loaded and unloaded along the building direction. To investigate the superelastic temperature range, samples were trained (200 cycles) with 6% nominal engineering strain to remove the phase transformation-induced plasticity [32]. In this work, samples with at least 85% recoverable strain ratio are considered to exhibit superelastic behavior.

3. Results

3.1. Evaluation of superelastic capability

The initiation of superelasticity is determined by the critical stress (σ_{SIM}) for stress-induced martensite transformation (SIMT).

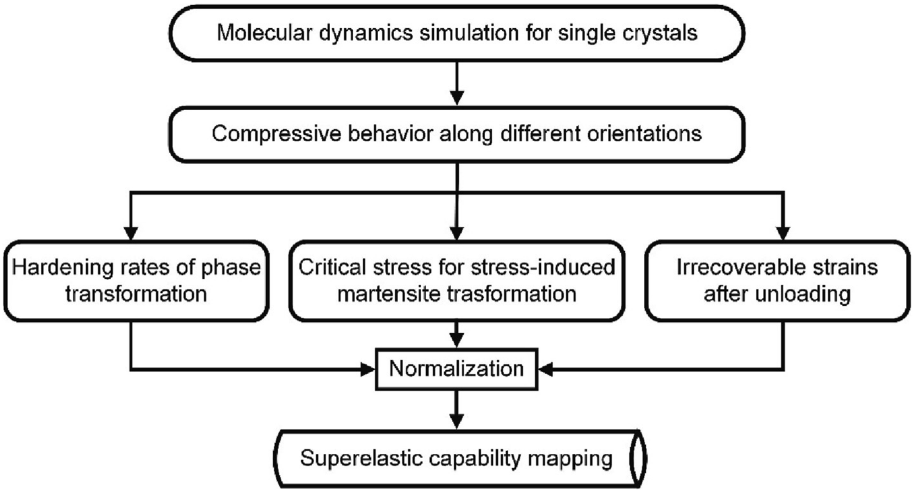

Fig. 2. A flowchart of the proposed screening method for desirable crystallographic orientations.

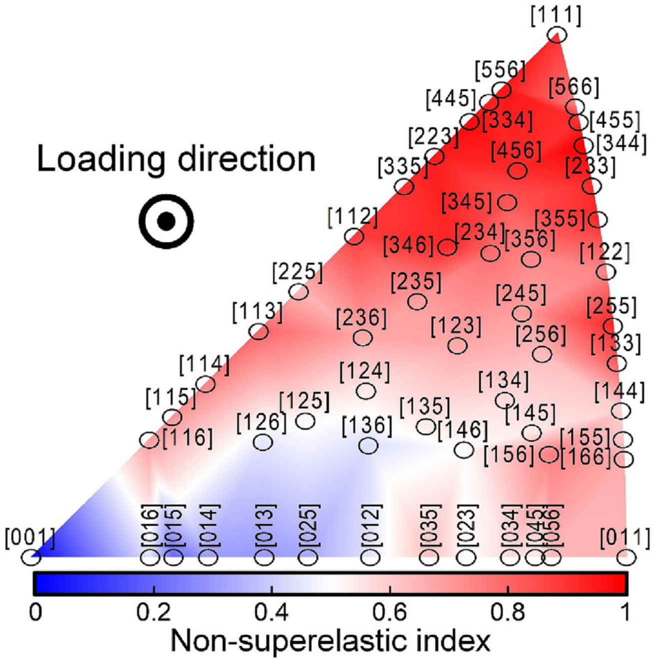

Fig. 3. The superelastic capability as a function of crystallographic orientation. The legend is, a dimensionless figure of merit to evaluate superelastic capability, non-superelastic index, and the smaller index value indicates better superelasticity.

Superelasticity disappearance occurs when the required stress of SIMT is higher than the critical stress for plastic slip (usually yield stress, σ_y). Desirable crystallographic orientations theoretically could make NiTi show a low hardening rate during SIMT, a relatively low σ_{SIM} and large recoverable strain.

To screen desirable NiTi crystallographic orientations, compression (at the test temperature 15 K above A_f) of single crystals was simulated by employing molecular dynamics (MD). In total, 55 crystallographic orientations were considered in this work and corresponding Miller indices are listed in Table S1 (in supplementary material), while the corresponding MD simulated compressive curves are shown in the supplementary Figure. S1. The screening process developed in this work is illustrated in a flowchart diagram (Fig. 2). To integrally evaluate the superelastic capabilities of NiTi with various crystallographic orientations, the hardening rate, σ_{SIM} and the irrecoverable strain were separately normalized by scaling between 0 and 1 to make it dimensionless. Then, the overall normalization was made based on the equal-weighted summation of the three factors as a dimensionless figure of merit to access superelastic capabilities. The lower value of the dimensionless figure of merit indicates the more desirable crystallographic orientation for releasing superelasticity.

For convenience, the dimensionless figure of merit is termed the “non-superelastic index”, and all calculated non-superelastic indices are summarized in an inverse pole figure (Fig. 3) (the corresponding normalized values are shown in Table S1). As shown in Fig. 3, only orientations close to [001] show high possibilities for desirable superelastic capabilities. Considering the fact that low-index orientations are more common in materials, the [001] orientated NiTi is selected to be further fabricated.

To further confirm the capability of ⟨001⟩ orientated NiTi of inducing superelasticity, three typical low-Miller-index bicrystal models with periodic boundary conditions, either ⟨001⟩, ⟨110⟩ or ⟨111⟩ orientations, were applied to simulate the compressive

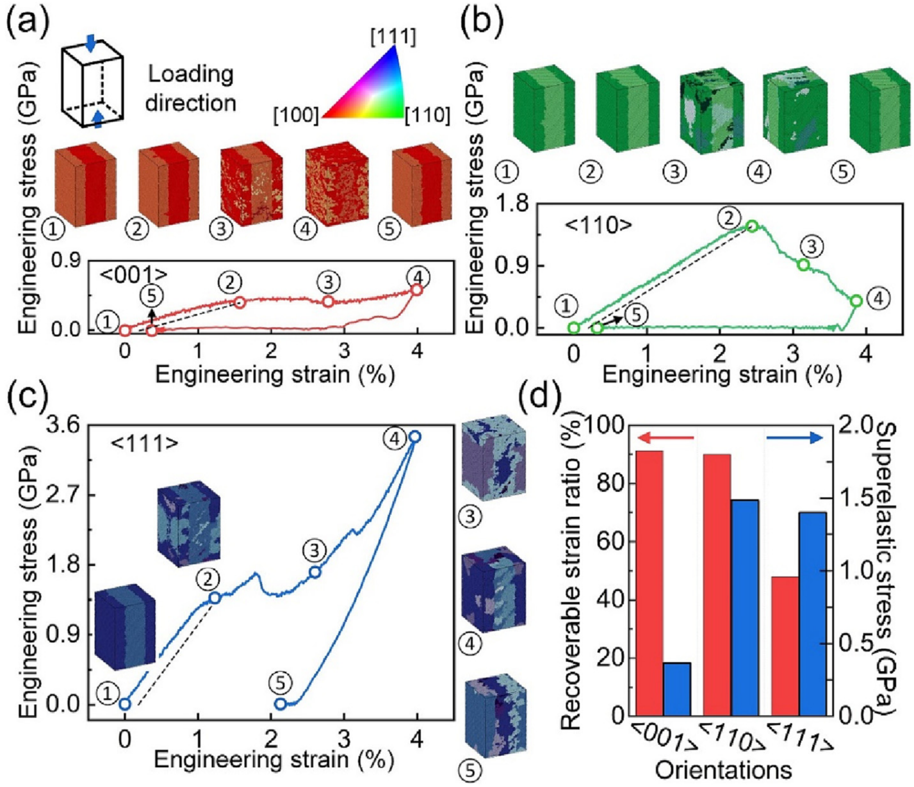

Fig. 4. MD simulations of 4% engineering strain compressive deformation of bicrystal NiTi periodic boundary conditions at 353 K, showing the behavior of (a) ⟨001⟩, (b) ⟨110⟩ and (c) ⟨111⟩ orientations; Corresponding simulated microstructures at different deformation stages are shown above the simulated stress–strain curves: ① the starting state, ② the critical point for stress-induced martensite transformation, ③ the intermediate state between ② and ④, ④ the position with 4% strain, and ⑤ the unloading state; the 0.2% strain offset method was used to identify critical stress for the stress-induced martensite transformation and different color domains within the simulated microstructures indicate grains with different orientations and martensite variants. (d) The recoverable strain ratios and superelastic stresses of various oriented models.

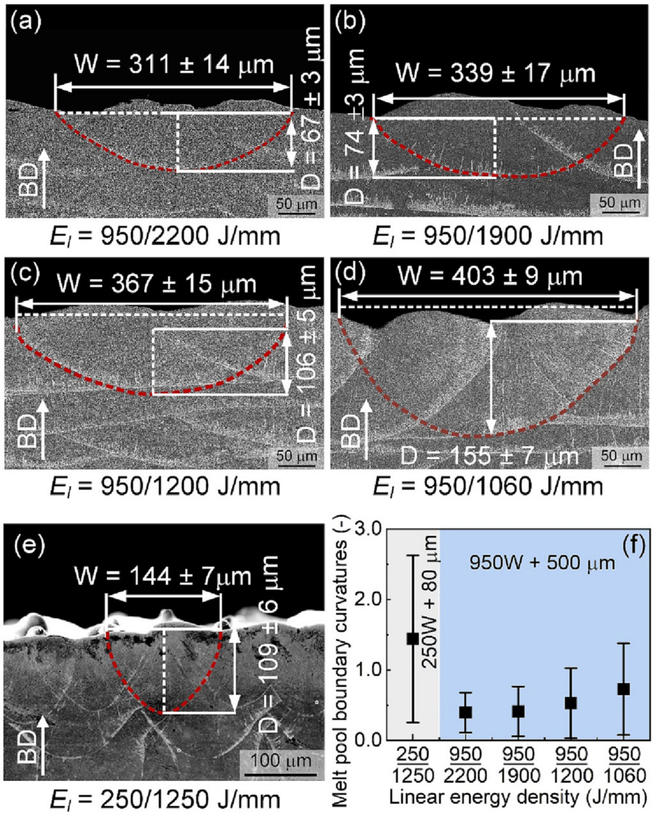

Fig. 5. (a)–(e) Cross-sectional L-PBF NiTi fabricated by various linear energy densities showing melt pool characteristics; (f) Cross-sectional melt pool boundary curvatures as a function of linear energy density.

behavior of polycrystalline NiTi. The ⟨001⟩ model shows the lowest σ_{SIM}, near-zero hardening rate and largest recoverable strain (Fig. 4 (a) and (d)), indicating a more favorable orientation for compression to activate SIMT and a better strain recoverability. Although the ⟨110⟩ orientation also shows superelasticity based on molecular dynamics results (Fig. 4 (b) and (d)), the high superelastic stress, SIMT instability (dropped stress during SIMT, Fig. 4 (b) ②–④), and large stress hysteresis may cause undesirable fatigue damage and low durability of functional parts [33]. For the ⟨111⟩ model, the high σ_{SIM} and hardening rate of SIMT results in more martensite variants (Fig. 4 (c) ④), which induces the interlocking effect of SIM variants and leads to poor strain recoverable ability after unloading. Therefore, it further demonstrates that NiTi with ⟨001⟩ orientated grains manifests a stable superelasticity.

3.2. Microstructure design and validation

The L-PBF process was employed to design ⟨001⟩ textured polycrystalline NiTi. In cubic crystal structured materials [34], solidified grains prefer to grow along ⟨001⟩ directions parallel to the local heat flow direction (NiTi has a body-centered-cubic structure at high temperature, BBC_B2) [34]. To fabricate NiTi with pronounced ⟨001⟩ texture, the thermal gradient direction should be parallel to the building direction (the layer-increasing direction) and columnar-shaped grains are required.

Grains grow parallel to the maximum thermal gradient perpendicular to solid–liquid interfaces (can be considered as melt pool boundaries) [35]. To ensure grain growth along the building direction to form a ⟨001⟩ texture, a wider and shallower melt pool is preferable for local thermal gradients with a consistent direction [36]. The featured melt pool can be achieved by applying a divergent laser beam with a positive defocus [37]. Here, a divergent laser beam with a 500 μm beam diameter was employed. To ensure sufficient energy input for creating stable melt pools, a 950 W laser power was used. The melt pool cross-sections for various linear energy densities ($E_l = \frac{P}{v}$, where P is laser power and v is scanning velocity) are shown in the Fig. 5 ((a)–(d)). The E_l of 950/1200 J/mm was chosen as it results in stable laser beads (Figure. S2 in supplementary materials) with wide and shallow melt pool cross-sections. For comparison, L-PBF NiTi fabricated with the commonly optimized E_l of 250/1250 J/mm is used as a reference [38], displaying a narrow and deep melt pool (Fig. 5 (e) and

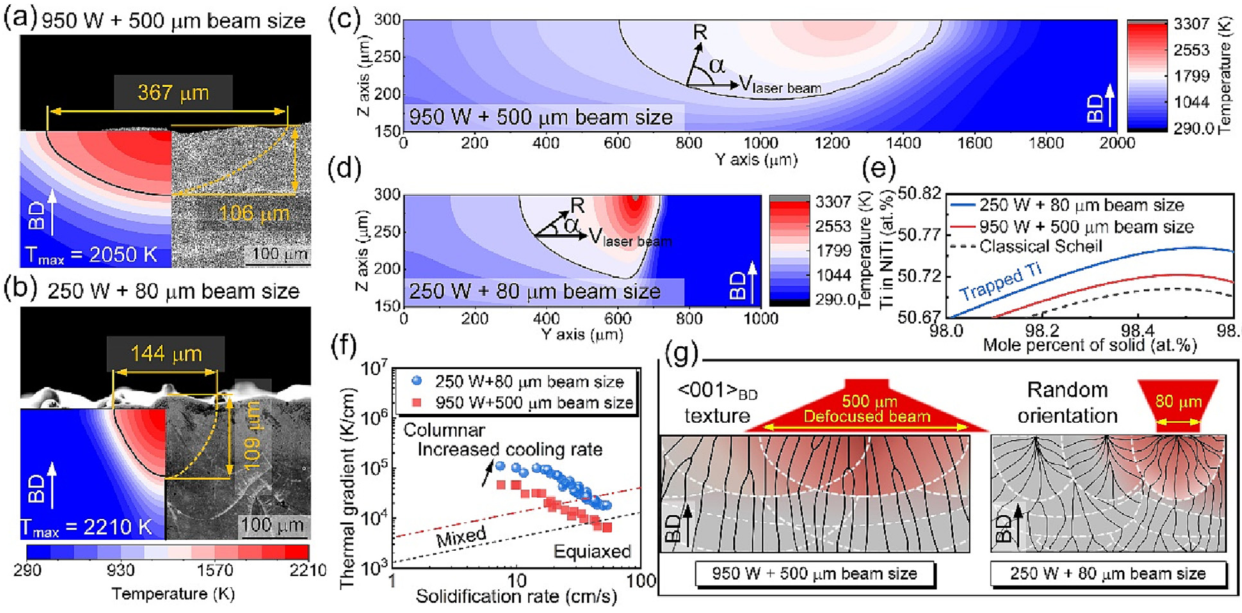

Fig. 6. Experimental and finite element simulated cross-sectional views of L-PBF NiTi melt pool characteristics for: (a) 950 W laser power with 500 μm beam diameter and (b) 250 W laser power with 80 μm beam diameter. Side-views (parallel to track deposition) of FEM simulated melt pools for (c) the processing condition of 950 W laser power, 1200 mm/s scanning velocity and 500 μm beam diameter and (d) the processing condition of 250 W laser power, 1250 mm/s scanning velocity and 80 μm beam diameter. (e) Ti in BCC NiTi phase as a function of the fraction of solid evaluated by a classic and solute trapping Scheil model. (f) Calculated microstructure selection map for Ni-Ti based on finite element analysis. (g) Schematic of grain growth over several deposition layers with two optimized processing conditions.

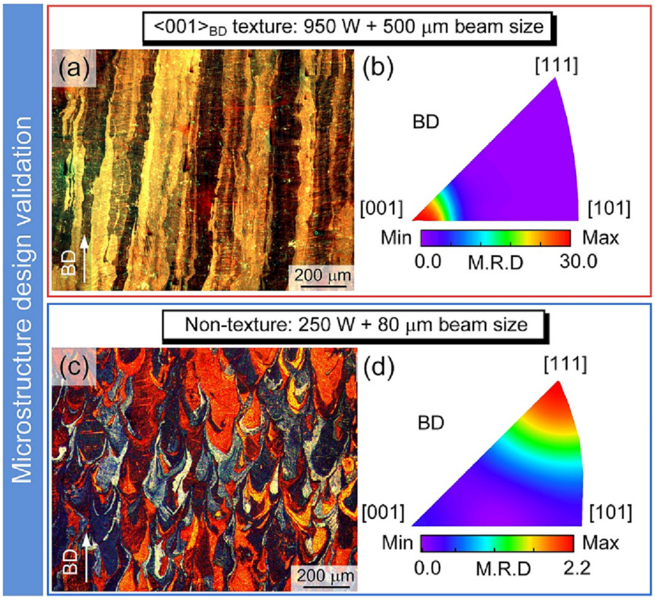

Fig. 7. Cross-sectional polarized light optical microstructure showing parent austenitic grains of L-PBF NiTi and inverse pole figures measured by XRD at 473 K to ensure fully austenitic BCC_B2 phase: (a) and (b) for 950 W laser power with 500 μm beam diameter; (c) and (d) for 250 W laser power with 80 μm beam diameter. M.R.D. stands for multiples of a random distribution.

(f)). For convenience, the processing condition of 950 W laser power, 1200 mm/s scanning velocity and 500 μm beam diameter is referred as the high laser power condition and the processing condition of 250 W laser power, 1250 mm/s scanning velocity and 80 μm beam diameter is referred as the low laser power condition.

To predict grain morphologies of L-PBF NiTi fabricated by using the optimized E_l of 950/1200 J/mm, finite-element modeling (FEM) and analytical modeling of grain morphology selection were conducted. Temperature fields, temperature gradients (values and directions) and melt pool shapes were predicted by FEM and the results obtained serve as further input for grain morphology prediction. Due to the large beam diameter, the energy input is more divergent, which results in smaller temperature gradients (Fig. 6 (a), (c), and (f)) than the low laser power condition (Fig. 6 (b), (d), and (f)). The simulated melt pool width and height match well with experimental results, indicating reliable FEM simulated results (Fig. 6 (a) and (b)).

The grain morphology selection is related to temperature gradients and solidification rates. The temperature gradients are extracted from FEM results and the solidification rates (R) are calculated based on the equation (1):

$$R = V_{\text{laser}} \times \cos\alpha \tag{5}$$

where V_{laser} is the laser beam scanning velocity and α is the angle between the local thermal gradient at the fusion boundary and the laser scanning direction. The developed grain morphology map shows that both applied processing conditions induce columnar grains (Fig. 6 (f)). Melt pool cross-sectional boundaries show that the high laser power coupled with a large beam size results in a small variation of fusion boundary curvature of ~ 0.5 (Fig. 5 (c) and (f), and Fig. 6 (a)). This promotes grain growth in a more consistent orientation along the building direction to form elongated ⟨001⟩ columnar grains. By contrast, the large melt pool boundary curvature of ~ 1.4 at the low laser power condition (Fig. 5 (e) and (f), and Fig. 6 (b)) leads to the frequent change of epitaxial grain growth direction with subsequent depositing layers, causing the formation of random texture. The grain growth behavior is illustrated in the Fig. 6 (g).

To validate our predictions, bulk NiTi parts were fabricated by L-PBF. To avoid structural defects in the high laser power condition, hatch distance (h) and layer thickness (t) were optimized based on our previously developed model as h = 180 μm and t = 50 μm (Figure. S3 in supplementary materials) [31]. For the low laser power condition, the common optimized processing parameters were applied for fabricating the reference NiTi sample [38]. As expected, the L-PBF NiTi with the high 950 W laser power condition shows columnar polycrystalline features with millimeter-scaled grains (length of ~ 2.5 mm, Figure. S4 in supplementary materials) and a strong ⟨001⟩ texture along the building direction (referred to $\langle 001\rangle_{BD}$ texture hereafter) (Fig. 7 (a) and (b)). The processing condition of low 250 W laser power with focused beam of 80 μm diameter leads to randomly oriented grains (Fig. 7 (c) and (d), referred to non-texture hereafter).

It should however be noted that despite the different grain orientations and sizes, the two materials show similar phase-transformation temperatures (Fig. 8 (a)) because phase-transformation temperatures are mainly controlled by the Ni content [15], which is ~ 49.4 ± 0.1 at.% (considered as Ni-lean,

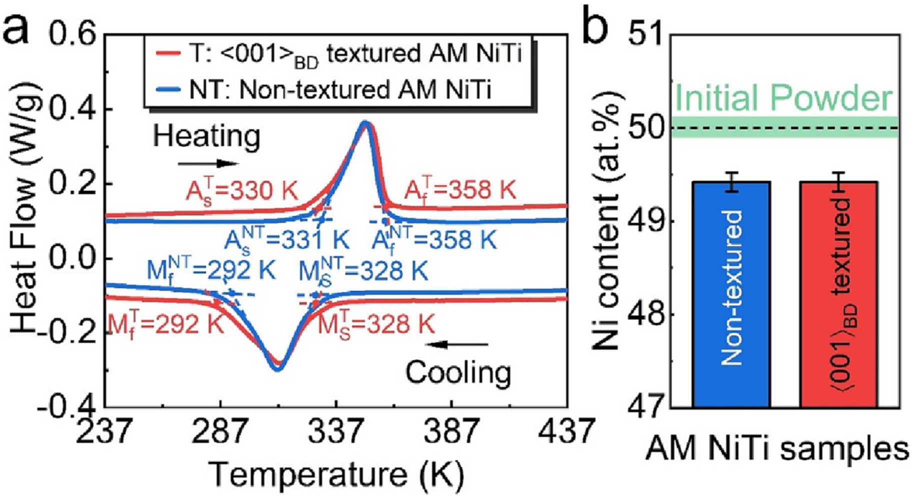

Fig. 8. (a) Differential scanning calorimetry (DSC) of as-fabricated $\langle 001\rangle_{BD}$ textured and non-textured AM NiTi; where, martensite start temperature is denoted as M_s, martensite finish temperature as M_f, austenite start temperature as A_s and austenite finish temperature as A_f. (b) Ni content of $\langle 001\rangle_{BD}$ textured and non-textured AM NiTi samples measured by inductively coupled plasma-optical emission spectrometry (ICP-OES) with 0.1 at.% accuracy. T is $\langle 001\rangle_{BD}$ texture and NT is non-texture.

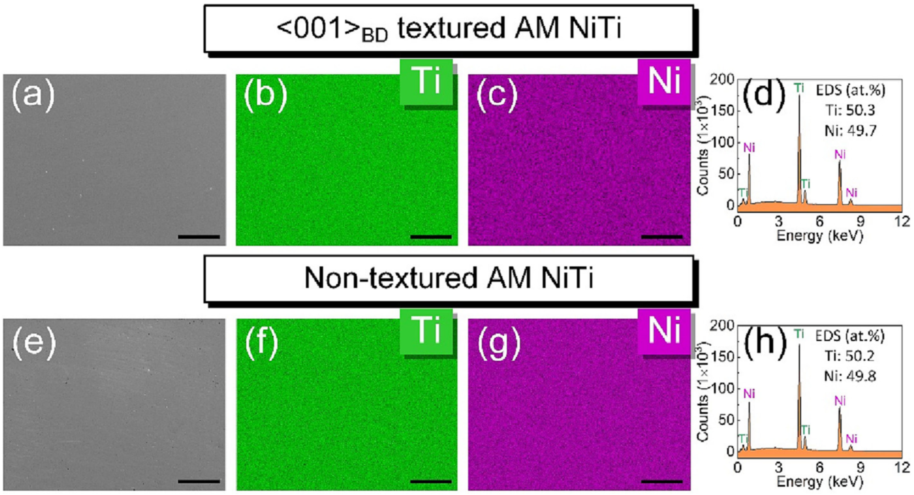

Fig. 9. (a) SEM image of $\langle 001\rangle_{BD}$ textured AM NiTi sample and its corresponding energy dispersive spectroscopy (EDS) maps of (b) Ti and (c) Ni and (d) EDS spectrum, showing homogeneous elemental distribution; (e) SEM image of non-textured AM NiTi sample and its corresponding energy dispersive spectroscopy (EDS) mappings of (f) Ti and (g) Ni and (h) EDS spectrum; All scale bars are 100 μm.

Fig. 8 (b)) for both fabrications. Notably, Ni-lean NiTi has previously always been considered as showing poor superelasticity, unless cold working coupled with complex heat treatments (HTs) were performed [39]. The $\langle 001\rangle_{BD}$ textured NiTi fabricated in this work also shows homogenous elemental distribution (Fig. 9), overcoming the drawback of element segregation with the directional solidification technique. In addition, the high laser power (950 W) coupled with a large beam size (500 μm) is not only promoting a desirable ⟨001⟩ texture formation but also improving the building rate (calculated by $v \times h \times t$) of NiTi AM fabrication from 4.5 to 10.8 mm^3/s.

3.3. Phase identifications and microstructure characterization

Considering the crystallographic textures in designed herein AM NiTi, a 2D-XRD technique was employed to identify phases.

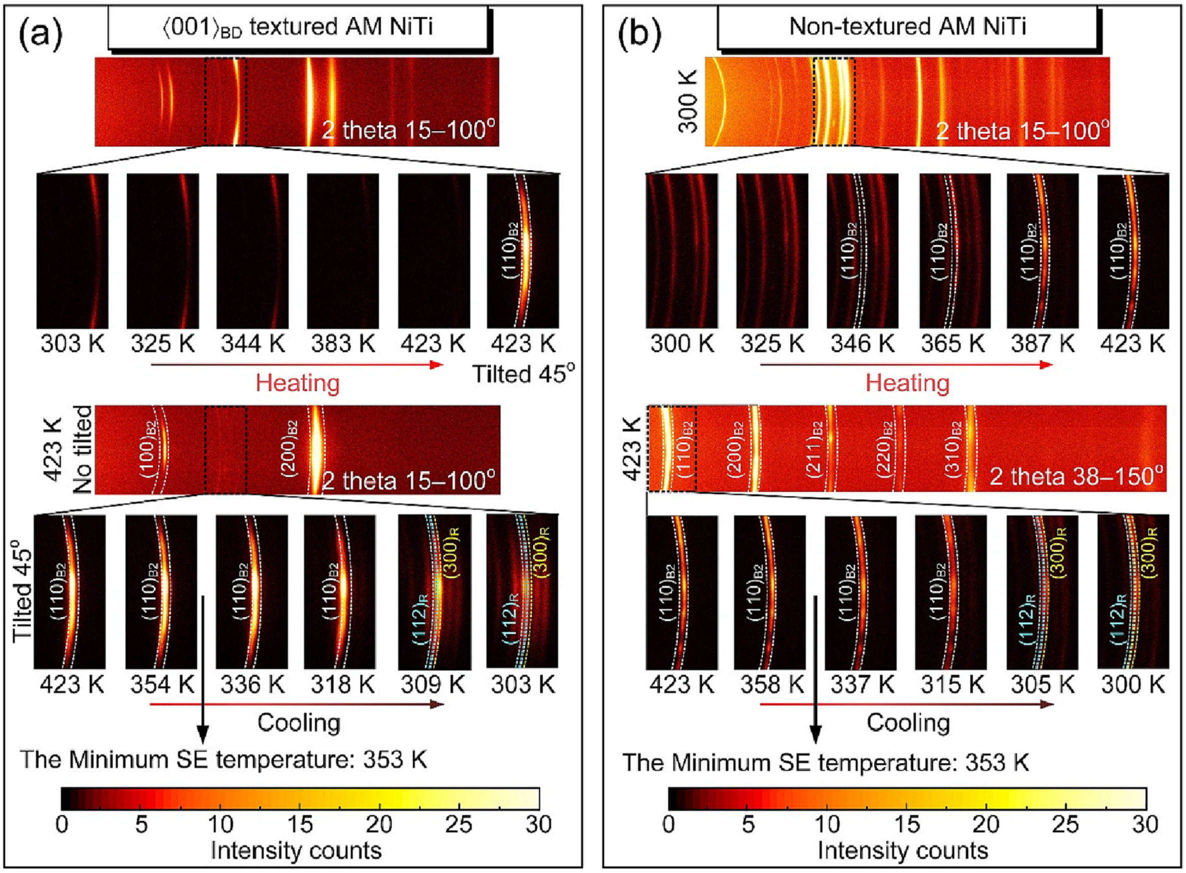

Fig. 10. In-situ heating and cooling two dimensional X-ray diffraction (2D-XRD) patterns: (a) non-textured and (b) $\langle 001\rangle_{BD}$ textured AM NiTi samples: Before superelasticity tests, samples were heated to 423 K and then cooled to testing temperatures (>353 K) to ensure an austenitic state (marked by black arrows in (a) and (b)). Only the austenite B2 phase and intermediate R phase were marked in 2D XRD patterns and the rest peaks are martensite B19′ phase.

At RT (~300 K), B19′ martensite is the main phase in both AM NiTi samples (Fig. 10). When the temperature is heated to 423 K, all B19′ martensite variants transform into B2 austenite phase. Since the strong [001] texture in the $\langle 001\rangle_{BD}$ textured sample, the $(110)_{B2}$ diffraction was shown after a 45° tilt relative to a horizontal plane (Fig. 10 (a)). Fewer Debye Scherrer diffraction rings and a strong single ring in the $\langle 001\rangle_{BD}$ textured sample indicate a preferred texture. For the cooling stage, the B2 → $M_{B19'}$ transformation occurs when the temperature is lower than 318 K (Fig. 10 (a)), which is consistent with DSC results (Fig. 8 (a)). With cooling back to RT, the R phase with a small fraction was detected (Fig. 10). The R phase is commonly seen in the NiTi and acts as an intermedia phase between B2 and B19′ phases [24]. Since the transformation temperature range of B2 → R is within the temperature range of B2 → B19′, the overlapped endothermic peaks cannot be observed by DSC (Fig. 8).

Employing different AM processing conditions also affects the morphology and width of the martensite (B19′) phase. The $\langle 001\rangle_{BD}$ textured AM NiTi (see Fig. 11 (a) and (c)) shows a ~ 10 times wider martensite spacing than the non-textured AM NiTi (Fig. 11 (b) and (d)). Besides, the $\langle 001\rangle_{BD}$ textured AM NiTi also shows a strong ⟨100⟩ and relatively weak ⟨011⟩ martensitic poles (Fig. 11 (e)). Based on the lattice correspondence of the $[001]_{B2}\|[100]_{B19'}$ and $[001]_{B2}\|[011]_{B19'}$ [40], the textured martensite phase (B19′) inherits the orientation from ⟨001⟩ textured austenite (BCC_B2) phase (Fig. 7 (d)).

In the nano-scale, the precipitate behavior in the as-fabricated $\langle 001\rangle_{BD}$ textured AM NiTi is quite distinct from that in the reference non-textured AM NiTi. Ti_2NiOx precipitates along grain boundaries were observed by TEM (Fig. 12 (a)–(c)) in the $\langle 001\rangle_{BD}$ textured AM NiTi. By contrast, only pure Ti particles formed within grains in the non-textured sample (Fig. 12 (d) and (e)).

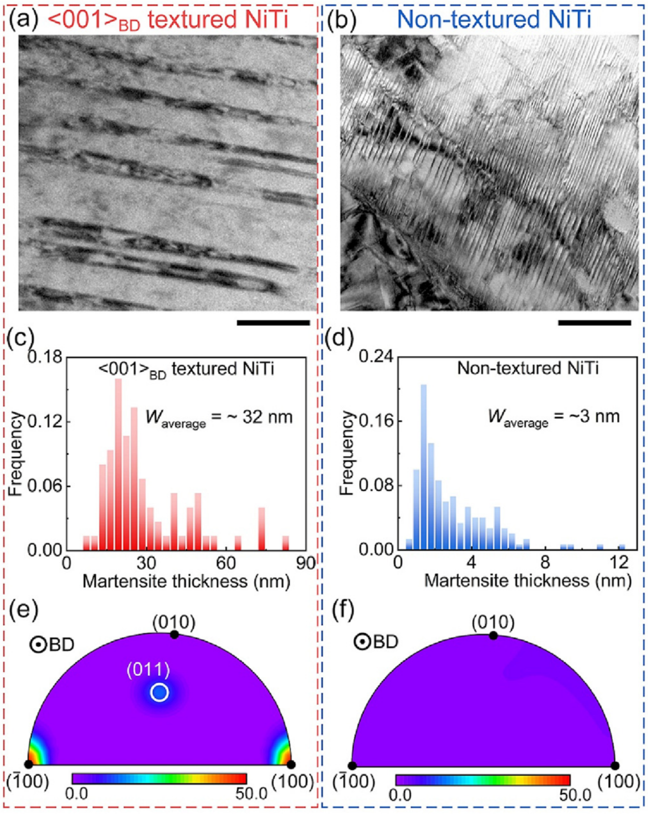

Fig. 11. Bright-field TEM images of (a, c)$\langle 001\rangle_{BD}$ textured and (b, d) non-textured AM NiTi samples, showing martensite size and morphology, and corresponding martensite width statistics; Inverse pole figures of B19′ martensite phase measured by XRD in (e) $\langle 001\rangle_{BD}$ textured and (f) non-textured AM NiTi samples measured at RT; All scale bars are 100 nm.

3.4. Functional properties of L-PBF NiTi

3.4.1. Superelasticity

To evaluate the superelasticity of AM NiTi with designed different textures, the samples were tested at 353 K (25 K above the martensite start temperature) to ensure a fully austenitic state (confirmed by in-situ two-dimensional X-ray diffraction, shown in Fig. 10). For the $\langle 001\rangle_{BD}$ textured NiTi, pronounced superelasticity was shown (the red line in Fig. 13 (a)). In contrast, the non-textured sample showed no superelasticity at 353 K (the red line in Fig. 13 (b)). It demonstrates the improved superelasticity in our designed $\langle 001\rangle_{BD}$ textured NiTi. To the best of the authors' knowledge, this superelasticity in a Ni-lean NiTi alloy is the first demonstrated for an AM material without any additional post processing.

To investigate superelastic temperature ranges, various loading temperatures were applied. The $\langle 001\rangle_{BD}$ textured AM NiTi shows superior superelasticity (4% recoverable strain from 353 K to 413 K) with a large temperature range of ~ 110 K and its highest superelastic temperature can reach up to 453 K (Fig. 13 (a)). As a comparison, the reference sample of the non-textured AM NiTi does not show any stable superelasticity from 343 to 373 K (Fig. 13 (b)), and it is already plastically deformed when tested above 363 K (Figure. S5 in supplementary materials**).** The achieved superelasticity in the $\langle 001\rangle_{BD}$ textured AM NiTi is remarkable as it is comparable with NiTi-Hf alloys [41]. Notably, NiTi-Hf alloys only have a narrow 20 K superelastic temperature range [42], while the textured NiTi designed in this work has a temperature window in excess of 5 times wider. It should be noted that the $\langle 001\rangle_{BD}$ textured AM NiTi partially loses its part of superelasticity when the temperature is higher than 413 K, and its recoverable strain ratio decreases to 86 % at 453 K. Such irrecoverable strain results from transformation- and reorientation-induced plasticity [43], which is due to the high stress level when test temperatures above 413 K (peak stresses > 750 MPa, Fig. 13 (a)).

3.4.2. Shape memory effect

The SME, as another important function of NiTi alloys, was also investigated. With a 4% compressive engineering strain, the $\langle 001\rangle_{BD}$ textured NiTi has almost 100% recoverable strain (Fig. 14 (a)) at the first SME cycle, that is if not considering the induced two-way shape-memory effect (illustrated in Fig. 1). The non-textured NiTi, as a comparison, has ~ 18% residual deformation (0.7% true strain) (Fig. 14 (b)). The $\langle 001\rangle_{BD}$ textured NiTi also shows better cyclic SME stability. After 50 SME cycles, the $\langle 001\rangle_{BD}$ textured NiTi still has ~ 1.6% recoverable strain, which is ~ 33% higher than the reference non-textured NiTi (Fig. 14 (c)). Even with the higher shape memory recoverable strain, the $\langle 001\rangle_{BD}$ textured NiTi still has comparable two way shape memory strain (~0.6) with the non-textured NiTi (Fig. 14 (d)).

4. Discussion

4.1. Occurrences of superelasticity in ⟨001⟩ textured NiTi

Our results clearly show that the achieved $\langle 001\rangle_{BD}$ texture can effectively induce superelasticity in Ni-lean NiTi. Based on the molecular dynamics simulation results, relatively low stress triggers stress-induced martensite transformation in ⟨001⟩ orientated grains (Fig. 3 and Fig. 4). This is due to the high resolved shear stress factor in ⟨001⟩ orientated NiTi [44,45]. As reported by Sehi-

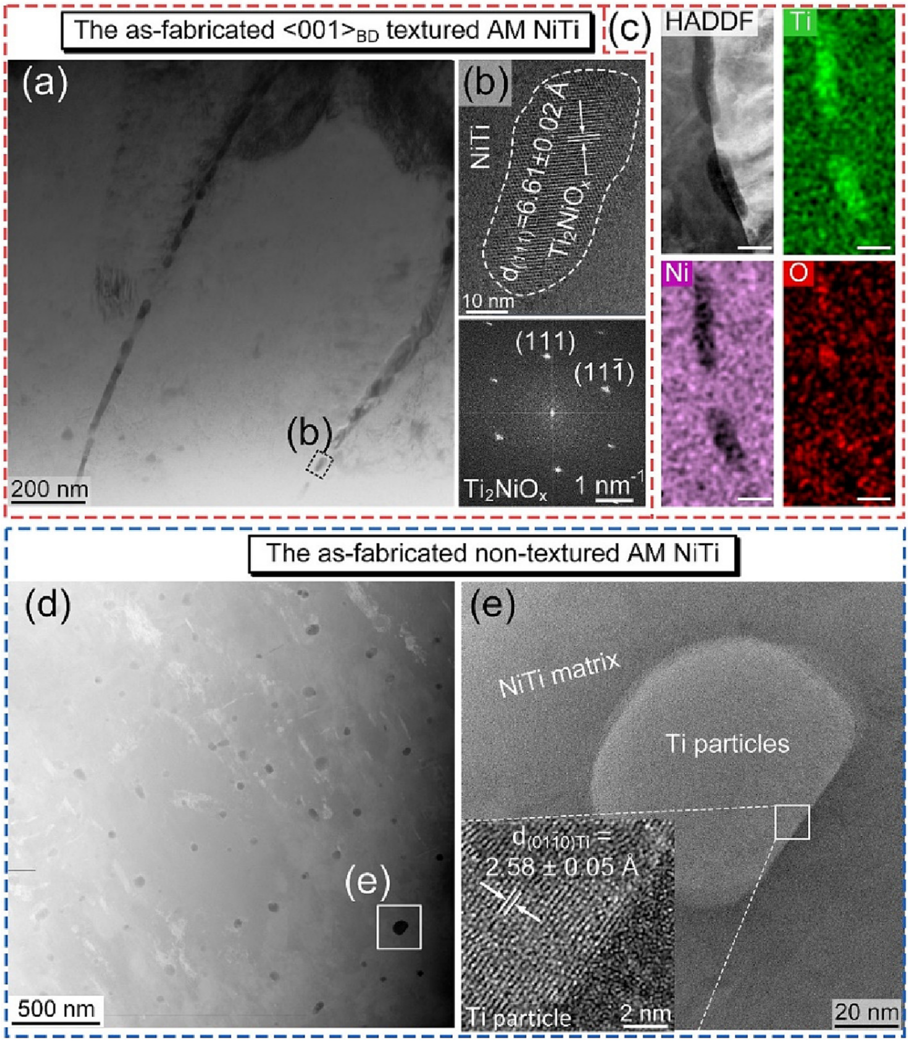

Fig. 12. (a) Bright-field TEM image of as-fabricated $\langle 001\rangle_{BD}$ textured NiTi sample. (b) HRTEM and corresponding fast Fourier transform (FFT) images of the $Ti_4Ni_2O_x$ precipitate in (b), and beam direction is close to $[1\ \bar{1}\ 0]$; (c) A HADDF image and corresponding EDS mappings of typical grain boundary precipitates. (d) High-angle annular dark field-scanning transmission electron microscopy (HAADF-STEM) images of the non-textured NiTi samples and (e) an enlarged precipitate observed by high-resolution transmission electron microscopy (HRTEM) with corresponding indexed result showing Ti particle in NiTi matrix (enlarged zone of (d), marked by a white square frame).

toglu *et al.*[45], the [001] single crystal has the lowest Schmid factors of austenite and martensite phases, which resulting in the enhanced recoverable strains and superelasticity. In this study, the fabricated polycrystalline $\langle 001\rangle$ orientated NiTi is single-crystal-like, hence, a superelastic behavior, similar with the [001] single crystal, was presented.

According to the post-translational modifications analysis, the deformed NiTi in the MD bicrystal models can be divided into different domains with different local lattice orientations. These domains were distinguished by various colors (Fig. 4 (a)–(c)). The number of domains can directly reflect the ability of coordinating deformation in MD bicrystal models with various orientations. The $\langle 001\rangle$ orientated NiTi shows the minimum number of 3 domains, indicating a good ability to coordinate deformation. Therefore, a relatively weak hardening effect is shown in the $\langle 001\rangle$ orientated NiTi during SIMT (Fig. 4 (a)). In experimental results, the SIMT in the $\langle 001\rangle_{BD}$ textured AM NiTi proceeds in a catalytic manner [46], i.e., showing a fluctuation feature during the SIMT (Fig. 13 (a)). This phenomenon further demonstrates that $\langle 001\rangle$ textured grains are more favorable for SIMT. By contrast, the non-textured AM NiTi containing some $\langle 111\rangle$ orientated grains shows no superelasticity. The reason can be attributed to the significant hardening effect, especially for $\langle 111\rangle$ orientated grains, during SIMT. The SIMT hardening is directly shown in the MD simulations and is also demonstrated by Sehitoglu *et al.* [45]. Due to the existence of six correspondent variant pairs, hardening effect is more pronounced in $\langle 111\rangle$ orientated grains, which leads to early yielding of the austenite and martensite phases and limited SIMT [45].

To understand why texture can control the occurrence of superelasticity even in NiTi with a Ni-lean composition, DSC tests were conducted on the two samples with distinct textures after 4% compressive deformation at 353 K. The DSC results showed additional shoulder peaks during heating (Fig. 15 (a) and (b)), indicating an increase in austenite-finish temperature. Especially for the non-textured sample (Fig. 15 (b)), the austenite-finish temperature of the deformed state (A_f^d) increases by 66 K to 424 K, compared with its initial non-deformed state ($A_f^{\text{Non - textured NiTi}} \approx A_f^{\langle 001\rangle_{BD}\text{textured NiTi}} = 358$ K). By contrast, there is

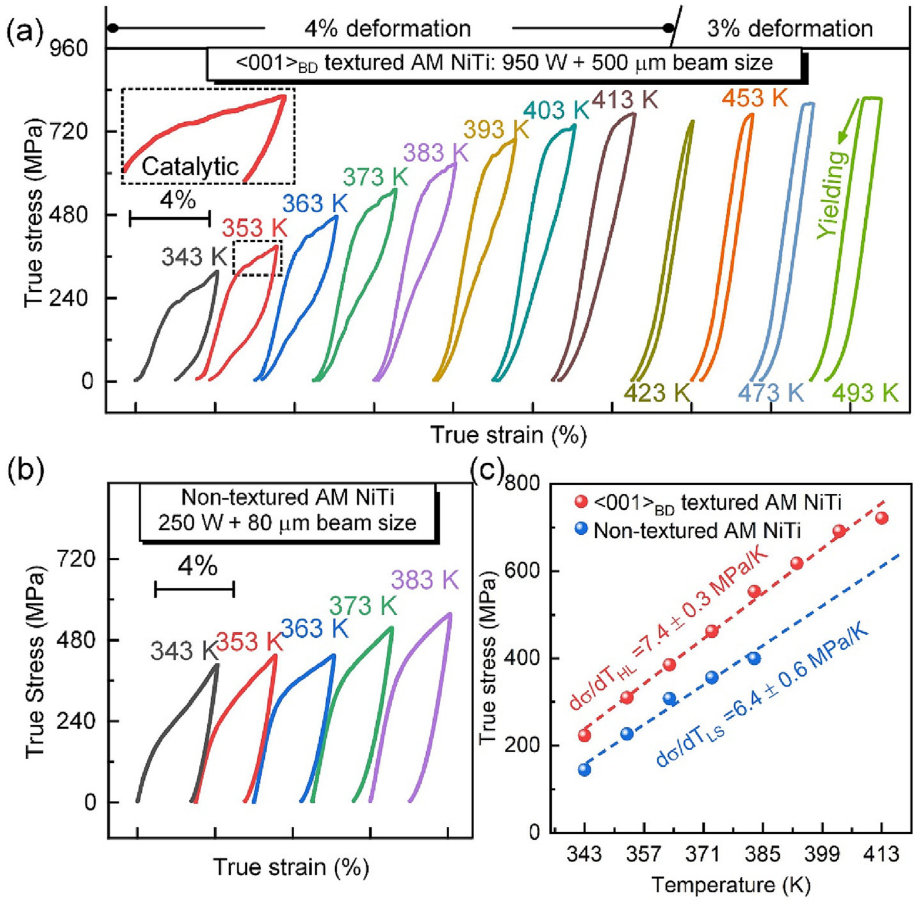

Fig. 13. True stress (σ_{true}) - true strain ($\varepsilon_{\mathrm{true}}$) curves as a function of temperatures for (a) $\langle 001\rangle_{\mathrm{BD}}$ textured and (b) non-textured samples. (c) The critical transformation stress as a function of test temperatures for $\langle 001\rangle_{\mathrm{BD}}$ textured and non-textured AM NiTi samples.

only a 26 K increase of A_f^d for the $\langle 001\rangle_{\mathrm{BD}}$ textured sample (Fig. 15 (a)). The DSC results indicate that lower reverse phase transformation resistance (stress-induced martensite to austenite) exists in the $\langle 001\rangle_{\mathrm{BD}}$ textured AM NiTi, leading to the occurrence of superelasticity.

To quantitatively evaluate the phase transformation compatibility between stress-induced martensite and austenite, the required additional austenite-finish temperature increments ($\Delta A_f = A_f^d - A_f$) were compared, and a lower ΔA_f means better phase transformation compatibility. The non-textured sample shows 2.5 times higher $\Delta A_f^{\text{Non - textured NiTi}}$ (66 K) and a higher fraction of 59% stress-induced martensite affected by deformation (the high disorder part in Fig. 15 (a) and (b)) than the $\langle 001\rangle_{\mathrm{BD}}$ textured sample ($\Delta A_f^{\langle 001\rangle_{\mathrm{BD}}\ \text{textured NiTi}}$=26 K and the high disorder part fraction is 11%). The result demonstrates that the designed $\langle 001\rangle_{\mathrm{BD}}$ texture is favorable for improving the SIMT compatibility between parent phases and the stress-induced martensite [47,48], which reduces the imposed elastic and interfacial energy resistance [49]. The improved compatibility in the $\langle 001\rangle_{\mathrm{BD}}$ textured AM NiTi directly promotes reverse transformation from stress-induced martensite to austenite during unloading at a constant temperature (Fig. 15 (c)), leading to the emergence of superelasticity. In contrast, the non-textured sample shows an irreversible transformation during unloading and the absence of superelasticity (Fig. 13 (b)), unless extra heating is induced to trigger the reverse transformation (Fig. 15 (d)).

4.2. Superelastic temperature ranges

Based on Clausius-Clapeyron relationship [18], the σ_{SIM} increases with increasing temperatures. Theoretically, the yield stress (σ_{y}) of NiTi decreases with increasing temperatures [50]. When above a critical temperature, $\sigma_{\mathrm{SIM}} > \sigma_{\mathrm{y}}$ occurs and the superelasticity is limited to below the critical temperature [50]. The high-temperature superelasticity with a wide temperature range requires low superelastic stress temperature dependence ($d\sigma_{\mathrm{SIM}}/dT$) and/or yield stress temperature dependence ($d\sigma_{\mathrm{y}}/dT$). In this work, the $\langle 001\rangle_{\mathrm{BD}}$ textured AM NiTi displays a relatively high superelastic stress temperature dependence ($d\sigma_{\mathrm{SIM}}/dT$) of ~ 7.4 MPa/K (Fig. 13 (c)). Hence, the high-temperature superelasticity could be attributed to the anti-yielding ability of the $\langle 001\rangle_{\mathrm{BD}}$ textured AM NiTi. The $\langle 001\rangle$ orientated NiTi crystal has the lowest Schmid factor of 0.00 in the typical NiTi $\langle 001\rangle\{110\}$ slip system [45] (Fig. 16), showing in theory no plastic slip. The MD single crystal model also demonstrates that the $\langle 001\rangle$ orientation also shows remarkable stability against yielding as a function of temperature (Fig. 17 (a)). In contrast, the $\langle 111\rangle$ orientation has a rapid decrease in yield stress (Fig. 17 (c)), which is consistent with results reported by Sehitoglu *et al.* [45]. In the non-textured NiTi, some grains also orientate along $\langle 111\rangle$ (a weak $\langle 111\rangle$ texture intensity of 2.2 in Fig. 7 (d)), which directly cause a poor superelastic response. Therefore, the exceptional anti-yielding ability of $\langle 001\rangle$ textured NiTi contributes to superior high-temperature superelasticity (up to 453 K) with a wide temperature range of ~ 110 K.

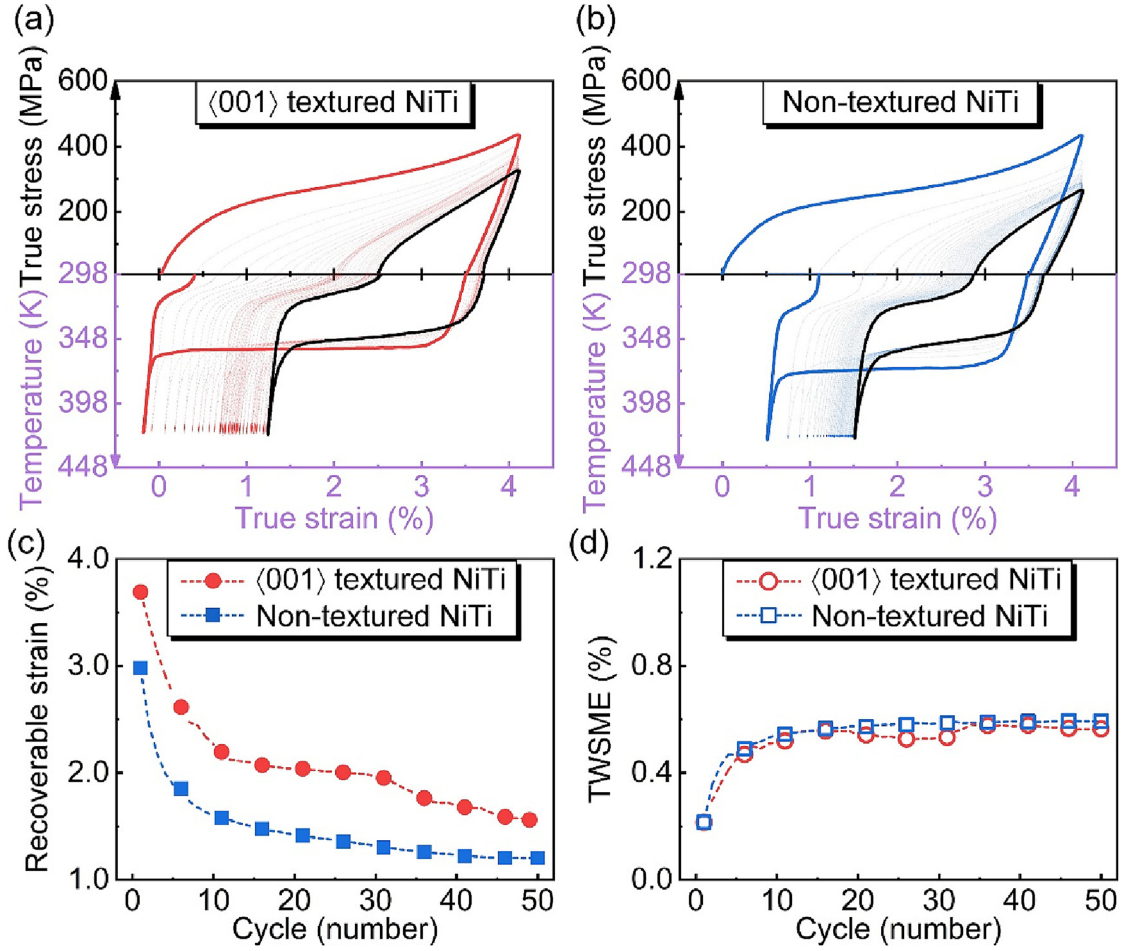

Fig. 14. True stress (σ_{true}) - true strain (ε_{true}) - temperature (T) curves of (a) as-fabricated $\langle 001\rangle_{BD}$ textured and (b) non-textured samples measured at RT showing shape memory effect. (c) The recoverable strain is a function of the number of cycles. (d) The two-way shape memory strain is a function of the number of cycles.

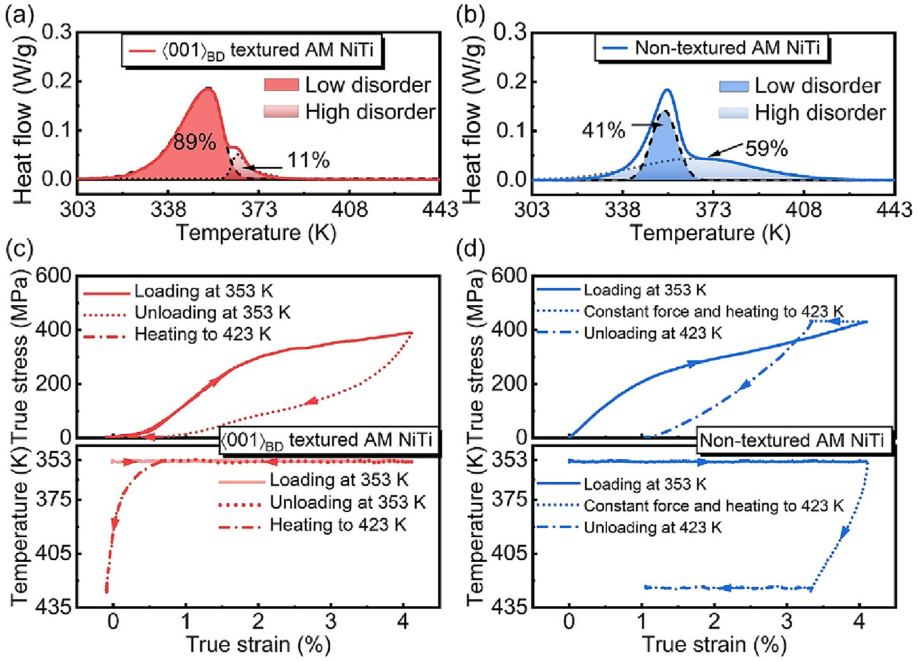

Fig. 15. Heating part of differential scanning calorimetry (DSC) curves for (a) the $\langle 001\rangle_{BD}$ textured and (b) the non-textured samples after 4% engineering strain under compression; True stress (σ_{true}) - true strain (ε_{true}) - temperature (T) curves of (c) the $\langle 001\rangle_{BD}$ textured NiTi (loading and unloading at 353 K and heating the sample to 423 K) and (d) the non-textured samples non-textured sample (loading at 353 K, constant applied force and heating the sample to 423 K, and unloading at 423 K).

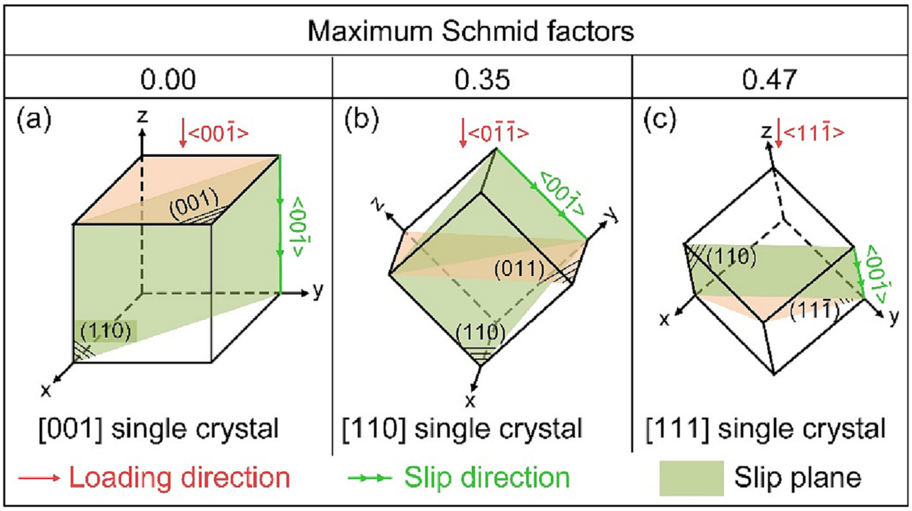

Fig. 16. Schematics of plasticity initiations with an activated $\langle 001\rangle\{110\}$ slip system [45] in BCC_B2 NiTi: Loading along a [0 0 1]; b [1 1 0]; and [1 1 1] directions.

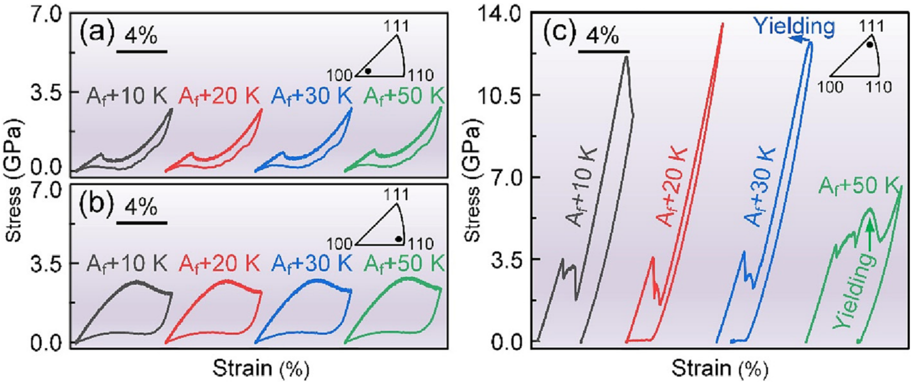

Fig. 17. MD simulated compressive strain (ε)-stress (σ) curves of single crystal NiTi with 8% engineering strain deformation at different temperatures, showing behavior for (a) [1 0 0], (b) [0 1 1] and (c) [1 1 1] orientations. All austenite finish temperatures (A_f) are 425 K.

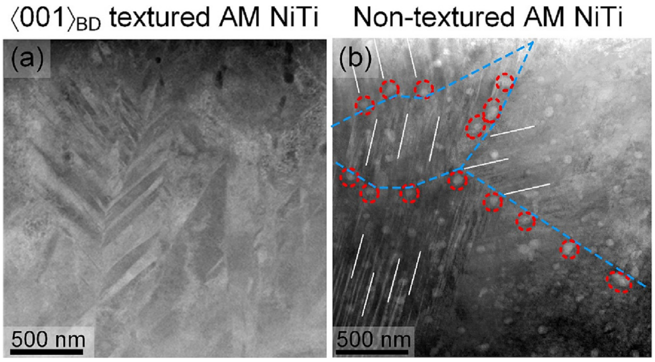

Fig. 18. Samples after 50 shape memory effect cycles: (a) a HAADF-STEM image of the $\langle 001\rangle_{BD}$ textured sample; (b) An annular dark-field STEM image in the non-textured sample and pure Ti particles were marked by red dash circles, martensite variant orientations were marked by solid white lines and different orientation zone were separated by blue lines. (For interpretation of the references to color in this figure legend, the reader is referred to the web version of this article.)

4.3. Stability of shape memory effect

A better shape memory recoverability and a higher SME cyclic stability were shown in the $\langle 001\rangle_{BD}$ textured AM NiTi as compared to the reference non-textured AM NiTi (Fig. 14). For the shape memory effect, the deformation stage is associated with the detwinning and reorientation of martensite variants, and deformation recovery is achieved by thermal-induced phase transformation via $M_{detwinned} \rightarrow A$. Due to inconsistent orientations of self-accommodated martensite before deforming and intrinsic lattice mismatch between austenite (BCC_B2) and martensite (B19′), dislocation and residual martensite accumulate to induce irrecoverable strain after cyclic SME tests [47,51]. In this work, a strong $\langle 100\rangle_{B19'}$ martensitic texture at RT, inherited from the $\langle 001\rangle_{B2}$ austenitic texture, was shown in the $\langle 001\rangle_{BD}$ textured AM NiTi. Such orientated martensite phases reduce interactions and interlocking effect of CVPs during detwinning and martensite reorientation resistance is also weakened accordingly. After cyclic SME tests, the martensite variants with greater width in the $\langle 001\rangle_{BD}$ textured AM NiTi (Fig. 18 (a)) indicate smaller internal stress and better compatibility between martensite and austenite [47]. By contrast, due to a higher internal stress in the cyclic SME tested non-textured AM NiTi, fine laminated martensite variants become dominant (Fig. 18 (b)).

Precipitation behavior also affects SME stability. In the $\langle 001\rangle_{BD}$ textured AM NiTi, grain boundaries decorated with Ti_2NiO_x precipitates block dislocation movements, which is seen in the TEM images (Fig. 19). By contrast, pure Ti particles formed within grains in the non-textured sample hinder martensite variant reorientations (Fig. 18 (b)) and cannot inhibit dislocation movement across grain boundaries. The precipitation behavior is determined by the

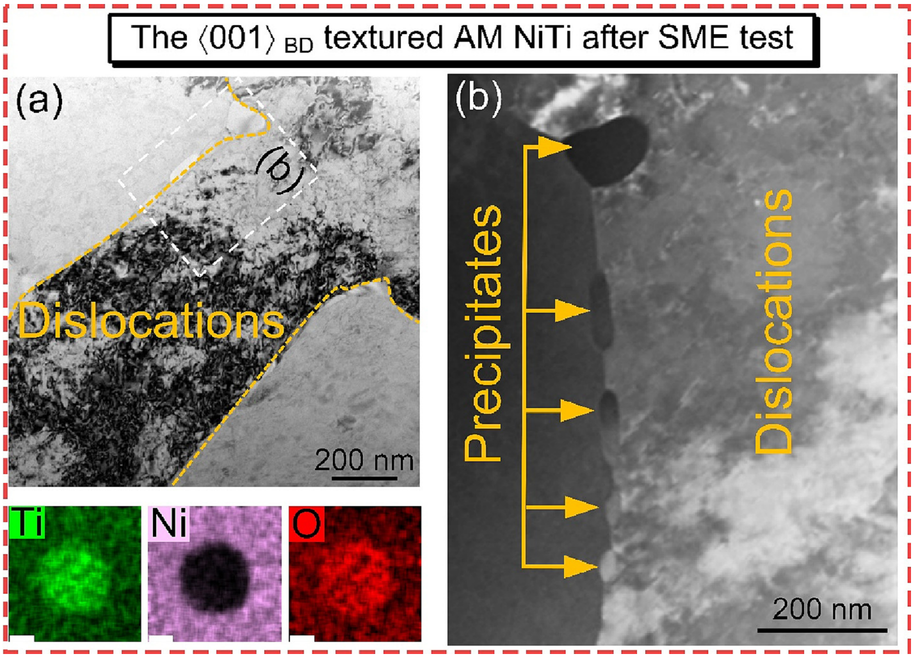

Fig. 19. (a) a bright field TEM image of the $\langle 001\rangle_{BD}$ textured sample after 50 shape memory effect cycles showing the dislocations pinned by precipitates segregated along the grain boundaries and energy-dispersive x-ray spectroscopy (EDS) maps of Ti, Ni, and O of a typical precipitate (all scale bars are 20 nm). (b) An enlarged HAADF-STEM image from a zone in (a).

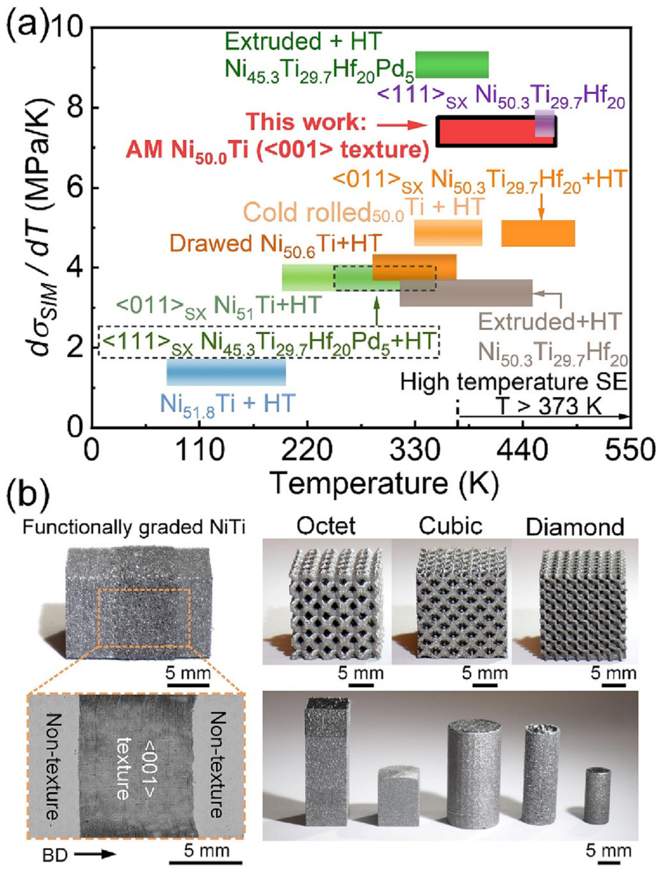

Fig. 20. (a) An overview of the superelastic temperature range (by temperature and the critical stress temperature dependence ($d\sigma_{SIM}/dT$)) for known NiTi-based alloys fabricated by different processes (SX, HT and SE are abbreviations of single crystal, heat treatment and superelasticity, respectively); (b) Examples of L-PBF–produced NiTi components including functionally graded parts, *meta*-structures and parts with different shapes (all scale bars are 5 mm).

solidification rate, which was calculated based on FEM and solute trapping Scheil models (Fig. 6 (c)–(f)). In the non-textured NiTi, a higher solidification rate results in more Ti being trapped into NiTi matrix and a more rapid cooling rate limits trapped Ti to react with NiTi to form $Ti_2Ni(O_x)$. Therefore, a better SME stability shown in the $\langle 001\rangle_{BD}$ textured AM NiTi attributes to the following two reasons: 1) the $\langle 100\rangle_{B19'}$ martensitic texture coordinates detwinning and reorientation of martensite variants; 2) intergranular precipitates pin dislocations.

4.4. Comparison of functional properties with other NiTi-based alloys

In this work, the wide superelastic temperature ranges, the high-temperature superelasticity, and the high critical stress temperature dependence allow binary Ni-lean NiTi to operate at elevated temperatures with wide tailorable stress windows (Fig. 20 (a)). The properties obtained are superior to complex multicomponent single crystal (SX) or polycrystalline NiTi-based alloys (such as NiTi-Hf and NiTi-Hf-Pd) fabricated by deformation processes coupled with long-time heat treatments (HT) [42,52]. By taking advantage of the additive manufacturing technique and using microstructure design concepts developed in this work, functionally graded NiTi and NiTi with complex metastructure geometries were successfully fabricated (Fig. 20 (b)). Such design flexibility opens a new path toward novel multifunctional and smart devices.

5. Conclusions

In summary, the proposed framework based on a synergy between finite-element, analytical and molecular-dynamic models, and additive manufacturing can help to achieve theory-guided microstructure and functional property design in NiTi SMAs. This discovery opens a new pathway to designing high-performance functional materials via additive manufacturing through controlling functional anisotropy. The specific conclusions are as follows:

1. The relationship between crystallographic orientations and superelasticity of NiTi SMAs has been studied via molecular dynamics, taking into account the critical stress for stress-induced martensite transformation, hardening rate during stress-induced transformation and recoverable strain. An orientation map of superelasticity has been drawn and crystallographic orientations close to ⟨001⟩ were found more favorable for superelasticity.
2. Based on predictions of temperature fields and grain morphologies, single-crystal-like polycrystalline Ni-lean NiTi with a strong ⟨001⟩ texture has been successfully fabricated via a laser powder bed fusion additive manufacturing technique.
3. An unprecedented superelasticity up to 453 K with a high and wide temperature window (~110 K) in a Ni-lean Ni (49.4 at. %)-Ti is achieved in the ⟨001⟩ textured additively manufactured NiTi, which is associated with the superior anti-yielding ability of the designed ⟨001⟩ texture and the improved phase transformation compatibility between austenite and stress-induced martensite.
4. The designed additive manufacturing processing condition can enhance superelasticity and improve shape memory stability simultaneously. The improved shape memory stability is attributed to the formation of ⟨100⟩ textured martensite and the dislocation movement blocked by grain decorated with Ti_2NiO_x precipitates.

CRediT authorship contribution statement

Jia-Ning Zhu: Writing – review & editing, Writing – original draft, Methodology, Investigation, Data curation, Formal analysis, Software, Validation, Conceptualization. **Kai Liu:** Writing – review & editing, Software. **Ton Riemslag:** Investigation, Conceptualization, Methodology. **Frans D. Tichelaar:** Writing – review & editing, Methodology, Investigation. **Evgenii Borisov:** Writing – review & editing, Methodology, Investigation. **Xiyu Yao:** Writing – review & editing, Methodology, Investigation. **Anatoly Popovich:** Writing – review & editing, Conceptualization. **Richard Huizenga:** Writing – review & editing, Methodology. **Marcel Hermans:** Writing – review & editing, Conceptualization. **Vera Popovich:** Writing – review & editing, Conceptualization, Project administration, Investigation, Funding acquisition, Supervision.

Data availability

No data was used for the research described in the article.

Declaration of Competing Interest

The authors declare that they have no known competing financial interests or personal relationships that could have appeared to influence the work reported in this paper.

Acknowledgments

The authors are grateful for the support from the Russian Science Foundation grant (project No. 19–79-30002). Jia-Ning Zhu wish to thank the China Scholarship Council (CSC) for financial support. Thanks to Mr. Sean Scott, Mrs. Elise Reinton and Zhaoying Ding for technical supports. We also thank Mr. D.P. Mainali for helping us with differential scanning analysis. The fruitful discussion of Professor Ian Richardson and Professor Jilt Sietsma on our manuscript are highly acknowledged.

Appendix A. Supplementary data

Supplementary data to this article can be found online at https://doi.org/10.1016/j.matdes.2023.111949.

References

[1] T. Omori, R. Kainuma, Alloys with long memories, Nature 502 (7469) (2013) 42–44.
[2] X. Ren, K. Otsuka, Origin of rubber-like behaviour in metal alloys, Nature 389 (6651) (1997) 579–582.
[3] E. Alarcon, L. Heller, E. de Prado, J. Kopeček, Temperature and microstructure dependent tensile behavior of coarse grained superelastic NiTi, Mater. Des. 226 (2023) 111617.
[4] D. Dye, Towards practical actuators, Nat. Mater. 14 (8) (2015) 760–761.
[5] X. Huang, G.J. Ackland, K.M. Rabe, Crystal structures and shape-memory behaviour of NiTi, Nat. Mater. 2 (5) (2003) 307–311.
[6] Y. Song, X. Chen, V. Dabade, T.W. Shield, R.D. James, Enhanced reversibility and unusual microstructure of a phase-transforming material, Nature 502 (7469) (2013) 85–88.
[7] J. Van Humbeeck, Shape memory alloys with high transformation temperatures, Mater. Res. Bull. 47 (10) (2012) 2966–2968.
[8] S. Li, D. Cong, Z. Chen, S. Li, C. Song, Y. Cao, Z. Nie, Y. Wang, A high-entropy high-temperature shape memory alloy with large and complete superelastic recovery, Mater. Res. Lett. 9 (6) (2021) 263–269.
[9] P. Hua, M. Xia, Y. Onuki, Q. Sun, Nanocomposite NiTi shape memory alloy with high strength and fatigue resistance, Nat. Nanotechnol. 16 (4) (2021) 409–413.
[10] H.E. Karaca, S.M. Saghaian, G. Ded, H. Tobe, B. Basaran, H.J. Maier, R.D. Noebe, Y.I. Chumlyakov, Effects of nanoprecipitation on the shape memory and material properties of an Ni-rich NiTiHf high temperature shape memory alloy, Acta Mater. 61 (19) (2013) 7422–7431.
[11] J. Zhang, T. Chen, W. Li, J. Bednarcik, A.-C. Dippel, High temperature superelasticity realized in equiatomic Ti-Ni conventional shape memory alloy by severe cold rolling, Mater. Des. 193 (2020) 108875.
[12] C.-H. Chen, Y.-J. Chen, Shape memory characteristics of (TiZrHf) 50Ni25Co10Cu15 high entropy shape memory alloy, Scripta Mater. 162 (2019) 185–189.
[13] H. Chen, F. Xiao, Z. Li, X. Jin, L. Mañosa, A. Planes, Elastocaloric effect with a broad temperature window and low energy loss in a nanograin Ti-44Ni-5Cu-1Al (at.%) shape memory alloy, Physical Review Materials 5 (1) (2021) 015201.
[14] X. Li, K. Lu, Improving sustainability with simpler alloys, Science 364 (6442) (2019) 733–734.
[15] J. Frenzel, E.P. George, A. Dlouhy, C. Somsen, M.F.X. Wagner, G. Eggeler, Influence of Ni on martensitic phase transformations in NiTi shape memory alloys, Acta Mater. 58 (9) (2010) 3444–3458.
[16] S. Saedi, A.S. Turabi, M. Taheri Andani, C. Haberland, H. Karaca, M. Elahinia, The influence of heat treatment on the thermomechanical response of Ni-rich NiTi alloys manufactured by selective laser melting, J. Alloys Compd. 677 (2016) 204–210.
[17] S.M. Saghaian, H.E. Karaca, H. Tobe, A.S. Turabi, S. Saedi, S.E. Saghaian, Y.I. Chumlyakov, R.D. Noebe, High strength NiTiHf shape memory alloys with tailorable properties, Acta Mater. 134 (2017) 211–220.
[18] J. Xia, Y. Noguchi, X. Xu, T. Odaira, Y. Kimura, M. Nagasako, T. Omori, R. Kainuma, Iron-based superelastic alloys with near-constant critical stress temperature dependence, Science 369 (6505) (2020) 855–858.
[19] X. Chong, M. Hu, P. Wu, Q. Shan, Y.H. Jiang, Z.L. Li, J. Feng, Tailoring the anisotropic mechanical properties of hexagonal M7X3 (M=Fe, Cr, W, Mo; X=C, B) by multialloying, Acta Mater. 169 (2019) 193–208.
[20] J.C. Guo, P. Rong, L. Wang, W.J. Chen, S.X. Han, R.N. Yang, X.W. Lei, W.J. Yao, N. Wang, A comparable study on stray grain susceptibilities on different crystallographic planes in single crystal superalloys, Acta Mater. 205 (2021) 116558.
[21] B. Blakey-Milner, P. Gradl, G. Snedden, M. Brooks, J. Pitot, E. Lopez, M. Leary, F. Berto, A. du Plessis, Metal additive manufacturing in aerospace: A review, Mater. Des. 209 (2021) 110008.
[22] S. Plimpton, Fast parallel algorithms for short-range molecular dynamics, J. Comput. Phys. 117 (1) (1995) 1–19.
[23] W.-S. Ko, B. Grabowski, J. Neugebauer, Development and application of a Ni-Ti interatomic potential with high predictive accuracy of the martensitic phase transition, Phys. Rev. B 92 (13) (2015) 134107.
[24] K. Otsuka, X. Ren, Physical metallurgy of Ti-Ni-based shape memory alloys, Prog. Mater Sci. 50 (5) (2005) 511–678.
[25] P. Hirel, Atomsk: A tool for manipulating and converting atomic data files, Comput. Phys. Commun. 197 (2015) 212–219.
[26] A. Stukowski, Visualization and analysis of atomistic simulation data with OVITO-the Open Visualization Tool, Modell. Simul. Mater. Sci. Eng. 18 (1) (2009) 015012.
[27] J.-N. Zhu, E. Borisov, X. Liang, R. Huizenga, A. Popovich, V. Bliznuk, R. Petrov, M. Hermans, V. Popovich, Controlling microstructure evolution and phase transformation behavior in additive manufacturing of nitinol shape memory alloys by tuning hatch distance, J. Mater. Sci. 57 (10) (2022) 6066–6084.
[28] P. Fischer, V. Romano, H.P. Weber, N.P. Karapatis, E. Boillat, R. Glardon, Sintering of commercially pure titanium powder with a Nd:YAG laser source, Acta Mater. 51 (6) (2003) 1651–1662.

[29] M. Tang, P.C. Pistorius, J.L. Beuth, Prediction of lack-of-fusion porosity for powder bed fusion, Addit. Manuf. 14 (2017) 39–48.

[30] M. Gäumann, C. Bezençon, P. Canalis, W. Kurz, Single-crystal laser deposition of superalloys: processing-microstructure maps, Acta Mater. 49 (6) (2001) 1051–1062.

[31] J.-N. Zhu, E. Borisov, X. Liang, E. Farber, M.J.M. Hermans, V.A. Popovich, Predictive analytical modelling and experimental validation of processing maps in additive manufacturing of nitinol alloys, Addit. Manuf. 38 (2021) 101802.

[32] S. Miyazaki, T. Imai, Y. Igo, K. Otsuka, Effect of cyclic deformation on the pseudoelasticity characteristics of Ti-Ni alloys, Metall. Trans. A 17 (1) (1986) 115–120.

[33] D. Wang, S. Hou, Y. Wang, X. Ding, S. Ren, X. Ren, Y. Wang, Superelasticity of slim hysteresis over a wide temperature range by nanodomains of martensite, Acta Mater. 66 (2014) 349–359.

[34] H.L. Wei, J. Mazumder, T. DebRoy, Evolution of solidification texture during additive manufacturing, Sci. Rep. 5 (1) (2015) 16446.

[35] E.H. Amara, R. Fabbro, Modelling of gas jet effect on the melt pool movements during deep penetration laser welding, J. Phys. D: Appl. Phys. 41 (5) (2008) 055503.

[36] M. Garibaldi, I. Ashcroft, M. Simonelli, R. Hague, Metallurgy of high-silicon steel parts produced using Selective Laser Melting, Acta Mater. 110 (2016) 207–216.

[37] J. Metelkova, Y. Kinds, K. Kempen, C. de Formanoir, A. Witvrouw, B. Van Hooreweder, On the influence of laser defocusing in Selective Laser Melting of 316L, Addit. Manuf. 23 (2018) 161–169.

[38] M. Elahinia, N. Shayesteh Moghaddam, M. Taheri Andani, A. Amerinatanzi, B.A. Bimber, R.F. Hamilton, Fabrication of NiTi through additive manufacturing: A review, Prog. Mater Sci. 83 (2016) 630–663.

[39] S. Miyazaki, My Experience with Ti-Ni-Based and Ti-Based Shape Memory Alloys, Shape Memory and Superelasticity 3 (4) (2017) 279–314.

[40] Y. Liu, The superelastic anisotropy in a NiTi shape memory alloy thin sheet, Acta Mater. 95 (2015) 411–427.

[41] G.P. Toker, M. Nematollahi, S.E. Saghaian, K.S. Baghbaderani, O. Benafan, M. Elahinia, H.E. Karaca, Shape memory behavior of NiTiHf alloys fabricated by selective laser melting, Scripta Mater. 178 (2020) 361–365.

[42] H.E. Karaca, S.M. Saghaian, B. Basaran, G.S. Bigelow, R.D. Noebe, Y.I. Chumlyakov, Compressive response of nickel-rich NiTiHf high-temperature shape memory single crystals along the [111] orientation, Scripta Mater. 65 (7) (2011) 577–580.

[43] C. Yu, G. Kang, Q. Kan, X. Xu, Physical mechanism based crystal plasticity model of NiTi shape memory alloys addressing the thermo-mechanical cyclic degeneration of shape memory effect, Mech. Mater. 112 (2017) 1–17.

[44] K. Gall, H. Sehitoglu, Y.I. Chumlyakov, I.V. Kireeva, Tension-compression asymmetry of the stress-strain response in aged single crystal and polycrystalline NiTi, Acta Mater. 47 (4) (1999) 1203–1217.

[45] H. Sehitoglu, I. Karaman, R. Anderson, X. Zhang, K. Gall, H.J. Maier, Y. Chumlyakov, Compressive response of NiTi single crystals, Acta Mater. 48 (13) (2000) 3311–3326.

[46] S.C. Mao, J.F. Luo, Z. Zhang, M.H. Wu, Y. Liu, X.D. Han, EBSD studies of the stress-induced B2–B19′ martensitic transformation in NiTi tubes under uniaxial tension and compression, Acta Mater. 58 (9) (2010) 3357–3366.

[47] J. Cui, Y.S. Chu, O.O. Famodu, Y. Furuya, J. Hattrick-Simpers, R.D. James, A. Ludwig, S. Thienhaus, M. Wuttig, Z. Zhang, I. Takeuchi, Combinatorial search of thermoelastic shape-memory alloys with extremely small hysteresis width, Nat. Mater. 5 (4) (2006) 286–290.

[48] P. Šittner, P. Sedlák, H. Seiner, P. Sedmák, J. Pilch, R. Delville, L. Heller, L. Kadeřávek, On the coupling between martensitic transformation and plasticity in NiTi: Experiments and continuum based modelling, Prog. Mater Sci. 98 (2018) 249–298.

[49] Y. Liu, S.P. Galvin, Criteria for pseudoelasticity in near-equiatomic NiTi shape memory alloys, Acta Mater. 45 (11) (1997) 4431–4439.

[50] A.S. Turabi, S. Saedi, S.M. Saghaian, H.E. Karaca, M.H. Elahinia, Experimental Characterization of Shape Memory Alloys, Shape Memory Alloy Actuators (2015) 239–277.

[51] K. Chu, Q. Sun, Reducing functional fatigue, transition stress and hysteresis of NiTi micropillars by one-step overstressed plastic deformation, Scripta Mater. 201 (2021) 113958.

[52] E.E. Timofeeva, N.Y. Surikov, A.I. Tagiltsev, A.S. Eftifeeva, A.A. Neyman, E.Y. Panchenko, Y.I. Chumlyakov, The superelasticity and shape memory effect in Ni-rich Ti-51.5Ni single crystals after one-step and two-step ageing, Mater. Sci. Eng., A 796 (2020) 140025.